Accepted Manuscript of: Laura Cervera-Gabalda, Anna Zielińska-Jurek, Cristina Gómez-Polo, Tuning the photocatalytic performance through magnetization in Co-Zn ferrite nanoparticles, Journal of Magnetism and Magnetic Materials, Volume 560, 2022, 169617, DOI: 10.1016/j.jmmm.2022.169617

Tuning of the photocatalytic performance through magnetization in Co-Zn ferrite nanoparticles

Laura Cervera-Gabalda[1,2], Anna Zielińska-Jurek[3], Cristina Gómez-Polo[1,2]

[1]Departamento de Ciencias, Universidad Pública de Navarra, Campus de Arrosadia, 31006 Pamplona, Spain.

[2]Institute for Advanced Materials and Mathematics (INAMAT^2), Universidad Pública de Navarra, Campus de Arrosadia, 31006, Pamplona, Spain.

[3]Department of Process Engineering and Chemical Technology, Gdansk University of Technology, Narutowicza 11/12, 80-233 Gdańsk, Poland.

Abstract.- In this work, the link between the photocatalytic performance of Co-Zn ferrite nanoparticles and the net magnetic moment of the spinel is analyzed. $Co_xZn_{1-x}Fe_2O_4$ nanoparticles ($0 \leq x \leq 1$) were synthesized by co-precipitation method. The physico-chemical properties were characterized by different structural and optical techniques (X-ray diffraction, Transmission Electron Microscopy (TEM), BET surface area, Diffuse Reflectance Spectroscopy (DRS), Photoluminescence spectroscopy, and Z-potential). Enhanced photocatalytic degradation (maximum degradation ratios of two emerging pollutants, phenol and toluene) are found for $0.4 \leq x \leq 0.6$, that cannot be explained in terms of the evolution of the analyzed physico-chemical parameters. However, the saturation magnetization (net magnetic moment) displays in the same compositional range maximum values as a result of the mixed inversion degree (cation distribution) of the spinel. Thus, nanoparticle magnetization is shown to be a key factor controlling photocatalytic response and supports the current open field linked to the magnetic field enhancement of photocatalytic applications.

(*) Corresponding autor.-
Prof. Cristina Gómez-Polo
Departamento de Ciencias. Edificio de los Acebos.
Universidad Pública de Navarra. Campus de Arrosadia. 31006 Pamplona. Spain
Phone. +34-948169576; e.mail: gpolo@unavarra.es

Keywords.- Co-Zn spinel ferrites; nanoparticles; superparamagnetism, photocatalytic; emerging pollutants

1. Introduction

Universal access to safe drinking water is currently a major challenge worldwide, being a fundamental need and human right. In 2020, three out of four people used safely managed drinking water services, however 771 million people still lacked even a basic level of service [1]. Despite extensive efforts in developing and implementing water reuse procedures, some persistent problems remain unsolved. Among them, the persistence of dangerous chemicals, such as highly persistent and toxic compounds (pesticides, herbicides, antibiotics, etc.) that cannot be adequately degraded by conventional techniques used in wastewater treatment procedures. In recent years, Advanced Oxidation Processes (AOPs), particularly photocatalysis have been proposed as promising procedures to remove persistent pollutants from the environment [2, 3]. In particular, heterogeneous photocatalysts based on semiconductor metal oxides (such as TiO_2 and ZnO) have demonstrated their efficiency in degrading a broad range of pollutants [4, 5]. Photocatalysis basically consists in the acceleration of a chemical reaction (decomposition of organic pollutants) as a result of the photogeneration of electron-hole pairs in the semiconductor material and the generation of highly reactive oxygen species e.g., hydroxyl radical, superoxide radical and singlet oxygen. Although this technique displays some advantages compared to conventional water remediation procedures (e.g., high efficiency and absence of secondary contamination), it has certain limitations that have reduced its implementation on a large scale. Particularly, low photoactivity under visible (solar) light and reduced quantum efficiency, which are primarily determined, respectively, by the wide band gap of the photocatalysts and a high recombination rate of photo-generated charge carriers. As an example, a widely employed photocatalyst as TiO_2 (band gap ~3.2 eV) is solely active under ultraviolet radiation, which only represents about 4% of the total solar radiation on the Earth surface.

Different strategies have been addressed to optimize the visible photocatalytic activity of semiconductor photocatalysts [6]: semiconductor doping (metal and non-metal) heterojunction with other semiconductors, modification with plasmonic structures, graphene carbon coatings, metal clusters or surface defects. Particularly, the optimization of photocatalytic response by thermal effects or through the application of external agents (i.e. electric field, stress or magnetic field) has also been reported in the literature [7]. Focussing on the magnetic field, its effect on the photocatalytic response is usually ascribed to the contribution of Lorentz and magnetohydrodynamic forces acting on the photogenerated charge carriers and chemical radicals [8-10]. Nevertheless, the intrinsic magnetic effect of the photocatalytic response of magnetic semiconductors should not be disregarded [11, 12]. Recent reports show the contribution of the magnetic state on the photocatalytic response of ferro and ferrimagnetic nanocatalysts, where the spin contribution in the redox phenomena should be taken into account [13, 14]. Besides, it has been shown how the spin polarization of the active catalyst surface controls and enhances the photocatalytic response in non ferromagnetic materials (i.e. defective TiO_2) [15, 16]. Thus, the topic is open to discussion and magnetic field effects on photocatalytic degradation is an active research field that requires further in-depth exploration.

Within the photocatalytic field, spinel ferrite photocatalysts have been extensively analyzed for the degradation of organic pollutants present in wastewater [17, 18]. Its optimum performance is achieved by the combination of a narrow band gap (within visible light range) and their ferrimagnetic nature that enables their reuse under several cycles through magnetic separation by the action of an external magnetic field [19, 20]. Among them, spinel Zn ferrite ($ZnFe_2O_4$) stands out due to the enhanced photochemical stability [21]. Visible-light photocatalytic performance has been reported in the degradation of different organic pollutants, as dyes [22], benzene [23], or phenol [24].

However, the main limitation regarding magnetic separation and photocatalyst reuse is its reduced magnetic moment (low saturation magnetization) in comparison with other spinel ferrites. In fact, bulk $ZnFe_2O_4$ is antiferromagnetic with Nèel temperature, $T_N = 10$ K, displaying reduced magnetic susceptibility at 300 K. Generally, the magnetic response of spinel ferrites is determined by the cation distribution between octahedral (B) and tetrahedral (A) sites of the face-centered cubic oxygen lattice. Bulk $ZnFe_2O_4$ is a *normal* spinel, where Fe^{3+} cations antiferromagnetically coupled occupy B, and Zn^{2+} cations (non magnetic) are preferentially located at the tetrahedral A positions [25]. The occurrence of *mixed* states (i.e., Fe^{3+} cations in both B and A sites) in Zn ferrite nanoparticles leads to ferrimagnetic behavior and the occurrence of characteristic superparamagnetism in the nanoscale regime [26]. Regarding, Co-Zn ferrites, maximum values in the saturation magnetization as a function of the Zn content are reported [27, 28] and ascribed to the redistribution of cation distribution between the octahedral and tetrahedral sites. Particularly, $CoFe_2O_4$ is an *inverse* spinel, where Co^{2+} cations tend to occupy B sites. As Co ions are replaced by Zn, a displacement of A-Fe^{3+} ions to the octahedral B-sites takes place. Since the octahedral B sites are twice the tetrahedral A sites and assuming the antiferromagnetic superexchange interaction much stronger than the ferromagnetic exchange within each A and B sublattices, an increase in the net magnetic moment takes place as Zn concentration increases. The further decay of the net magnetic moment for Zn-rich ferrites is ascribed to the null magnetic moment of Zn^{2+} ions (null value of unpaired 3d electrons). Furthermore, the inversion degree (distribution of octahedral and tetrahedral cations in the spinel lattice) also determines the semiconductor band structure, particularly the band gap energy and thus the irradiation wavelength to activate efficient visible photocatalytic activity [29, 30]. However, despite previous studies on Zn-Co spinel nanoparticles, the magnetic contribution of these systems to the photocatalytic phenome is hardly analyzed in the literature.

In this context, the aim of the work is to study the link between the photocatalytic performance of Zn-Co ferrite nanoparticles to their magnetic response, specifically the net magnetic moment of the spinel lattice. $Co_xZn_{1-x}Fe_2O_4$ nanoparticles ($0 \leq x \leq 1$) were synthesized by the co-precipitation method, and their physicochemical properties were characterized by different structural and optical techniques (crystal structure, mean nanoparticle size, specific surface area, isoelectric point, optical absorption, photoluminescence). The results show an improvement of the visible photocatalytic performance (maximum degradation ratios) for Co-Zn nanoparticles ($0.4 \leq x \leq 0.6$) with optimum magnetic response (room temperature superparamagnetism and high net magnetic moment).

2. Experimental Procedure

2.1 Synthesis of photocatalysts

Following the procedure described in [28], the synthesis of $Co_xZn_{1-x}Fe_2O_4$ nanoparticles ($0 \leq x \leq 1$) was carried out by the co-precipitation method. Briefly, $Fe(NO_3)_3 \cdot 9H_2O$, $Zn(NO_3)_2 \cdot 6H_2O$, and $Co(NO_2)_3 \cdot 6H_2O$ were mixed stoichiometrically in an aqueous solution. Then, NaOH solution (1 M) was added dropwise under constant stirring until the pH was 13, allowing the precipitation and complete hydrolyzation of the ions. The precipitate was collected by centrifugation, washed, and dried at 50 ^{0}C overnight. Finally, the samples were calcined at 400 ^{0}C for 6 hours.

2.2 Characterization of photocatalysts

X-ray powder diffraction (XRD) patterns of $Co_xZn_{1-x}Fe_2O_4$ nanoparticles were recorded at room temperature on a Siemens D-5000 diffractometer with a CuKα radiation source and operated at 30 mA and 40 kV. Additionally, X-ray fluorescence (XRF) was employed to determine the composition of the samples (THERMO ELECTRON ARL mod. ADVANT'XP). The nanoparticle morphology and size distribution were analyzed through Scanning Transmission Electron Microscopy (STEM) with a high angle annular dark field detector, STEM-HAADF (Tecnai Field Emission Gun operated at 300 kV). Adsorption-desorption curves of nitrogen at 77 K were employed (Brunauer–Emmett–Teller, *BET*, method) to determine the specific surface areas and pore distribution on a Micrometrics Gemini V (model 2365) instrument. The isoelectric point of the nanoparticles was characterized through the analysis of the Zeta potential at different pH employing HCl 0.1M and NaOH 0.1M to adjust the pH (Malvern Instruments Zetasizer 3000). Regarding the optical characterization of the samples, Diffuse Reflectance Spectroscopy (DRS) were recorded by UV/Vis/NIR Jasco V-670 to evaluate the band gap energy calculated using the Kubelka-Munk function. A Perkin Elmer LS55 spectrophotometer was employed in the characterization of the Photoluminescence (*PL*) emission spectra. The *PL* emission spectrum was recorded at room temperature in the range of 300 – 700 nm with an excitation wavelength of 250 nm. Finally, magnetic measurements were performed with a SQUID magnetometer (Quantum Design MPMS XL7), enabling the characterization of the temperature dependence (5 – 300 K) of the magnetization and the hysteresis loops of the samples.

2.3 Photocatalytic activity measurements

To study the photocatalytic activity of the Co-Zn ferrites in an aqueous solution, phenol was used as a model organic contaminant in water. The suspension of Co_xZn_{1-}

$_{x}Fe_2O_4$ nanoparticles (pH = 7) prepared by mixing 24 cm^3 of water, 1 cm^3 of phenol solution (500 mg/dm^3), and 50 mg of catalyst was stirred for 30 min and aerated (V = 5 dm^3/h) in the dark to obtained equilibrium. Then the suspension was photoirradiated with a 300 W Xenon lamp (Oriel). The optical path included a water filter and glass filter GG400 to cut off IR and Vis irradiation. GG glass filter transmitted light of wavelength greater than 400 nm. The photoreactor (V = 25 cm^3) was equipped with a quartz window, and the exposure layer thickness was 3 cm. The temperature of the aqueous phase during irradiation was set at 20°C using a water bath. Then, aliquots collected at different times of reaction, with and without irradiation, were analyzed by reverse-phase high-performance liquid chromatograph Shimadzu LC-6A (Kyoto, Japan) with photodiode array detector Shimadzu SPD-M20A to determine the phenol concentration. The measurements were performed using a C18 column (Phenomenex Gemini 5 µm; 150x4.6 mm) working at 45 °C under isocratic flow conditions of 0.3 cm^3·min^{-1}. During HPLC measurements, mobile phase composed of (v/v) 70% acetonitrile, 29.5% water, and 0.5% orthophosphoric acid (85% w/w solution) was used at the flow rate of 0.3 cm^3·min^{-1}.

Toluene was used as a model air contaminant. The gaseous mixture was prepared by dropping a certain amount of liquid toluene into the valve of an empty steel gas tank and subsequently filling the tank with air until gas pressure reached 20×10^5 Pa. The concentration of toluene in the gas mixture was about 200 ppm. The photodegradation tests were carried out in a flat stainless steel reactor with a working volume of about 30 cm^3. The reactor was equipped with a quartz window, two valves, and septa. An array of 25 LEDs (λ_{max}= 415 nm, 63 mW per diode) was applied as an irradiation source. In a typical photocatalytic activity measurement, a glass plate (25 mm × 25 mm) coated with the $Co_xZn_{1-x}Fe_2O_4$ photocatalyst layer was placed at the bottom side of the reactor followed by closing the reactor with a quartz window. Prepared suspension of the photocatalyst (0.02 g) in water was applied to the glass plate and dried at room temperature. In the first measuring cycle, the gaseous mixture was passed through the reaction space for 20 min. After closing the valves, the reactor was kept in the dark until toluene concentration remains stable. Then, the sample irradiation starts. The analysis of toluene concentration in the gas phase was performed using a gas chromatograph (Clarus 500, PerkinElmer) equipped with a flame ionization detector (FID) and Elite-5 capillary column (30 m × 0.25 mm, 0.25 μm). The samples (200 μl) were dosed by using a gas-tight syringe. Nitrogen 1 cm^3/min was used as the carrier gas.

3. Results and discussion

3.1 Structural characterization

Firstly, the crystal structure of synthesized $Co_xZn_{1-x}Fe_2O_4$ nanoparticles was analyzed by X-ray diffraction. The structural parameters were calculated by Rietveld refinements [31], where patterns were fitted assuming a cubic spinel structure ($Fd\bar{3}m$ space group. For the refinement, the cation positions were fixed in two crystallographic sites, tetrahedral A site (x=y=z=0.125) and octahedral B site (x=y=z=0.5), assuming the distribution of Co, Fe, and Zn in these two available crystallographic sites. The cation occupancy in A and B sites was refined as well as the background, 2θ zero, scale factor, peak profile, oxygen position, and the cell parameter. Figure 1 depicts, as examples, the measured and calculated X-ray diffraction patterns for x = 0, 0.3, 0.6 and 1. The samples display a single cubic spinel structure with the exception of x = 0 ($ZnFe_2O_4$), where a fraction of ZnO ($P6_3mc$ space group) as secondary phase (12 wt%) is also detected. Table I summarizes the Rietveld fitted cell parameters of the cubic spinel ($Fd\bar{3}m$) for the calcined nanoparticles. As previously reported [28, 32-34] a decreasing trend in the lattice constant is found as Co content (x) increases, as a consequence of the larger ionic radius of Zn^{2+} in comparison with the Co^{2+} cation. Furthermore, the relative metal composition for the Co-Zn mixed ferrites was checked through X-ray florescence (XRF), see Table I. No significant differences are detected between the nominal composition of the Co-Zn nanoparticles and the final composition after the calcination procedure.

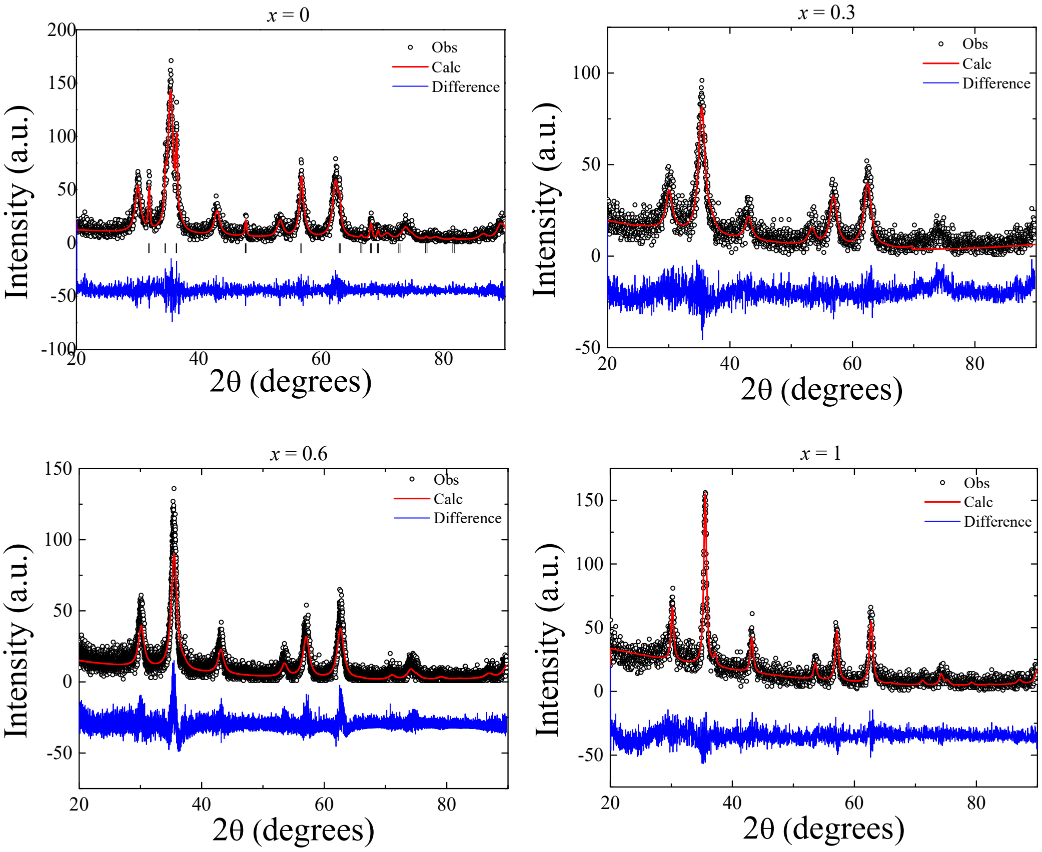

Figure 1. Rietveld adjustments for $Co_xZn_{1-x}Fe_2O_4$ nanoparticles ($x = 0$, 0.3, 0.6 and 1) (o) experimental and (—) calculated intensities. The difference between both intensities is shown at the bottom of the figures (—). The Bragg reflections of ZnO are shown (|).

Regarding the mean crystallite size, *d*, estimated through Scherrer equation, an opposite trend is found with *x*, that is, an increase as the Co content (*x*) increases [32, 35]. As Table I summarizes, *d* ranges from 5 to 13 nm for $x = 0$ and 1, respectively, confirming the nanometric dimensions of the calcined materials.

Table I. Estimated XRF cation composition, lattice parameters obtained from XRD Rietveld refinement, crystallite and STEM mean sizes for the $Co_xZn_{1-x}Fe_2O_4$ calcined nanoparticles.

***Nominal Co content** (x)*	***Composition (XRF)***	***Cell parameters** (Å) a=b=c*	***Crystallite size** (nm)*	***STEM mean size** (nm)*
0		8.428(1)	5.138(0.003)	8.9±1.3
0.1	$Co_{0.1}Zn_{0.9}Fe_{1.94}O_4$	8.4105(5)	6.050(0.002)	8.4±1.3
0.3	$Co_{0.36}Zn_{0.64}Fe_{2.05}O_4$	8.408(1)	4.720(0.002)	7.1±1.2
0.4	$Co_{0.41}Zn_{0.59}Fe_{1.95}O_4$	8.3594(7)	7.267(0.002)	9.0±1.3
0.5	$Co_{0.48}Zn_{0.52}Fe_{1.90}O_4$	8.3781(5)	6.66(0.05)	7.9±1.3
0.6	$Co_{0.59}Zn_{0.41}Fe_{1.91}O_4$	8.3879(6)	5.445(0.002)	9.2±1.3
0.7	$Co_{0.68}Zn_{0.32}Fe_{1.86}O_4$	8.350(1)	7.331(0.004)	8.2±1.3
0.9	$Co_{0.89}Zn_{0.11}Fe_{1.87}O_4$	8.351(1)	9.187(0.004)	13.0±1.4
1.0		8.377(1)	13.072(0.008)	19.0±1.3

The surface morphology and the size distribution of the $Co_xZn_{1-x}Fe_2O_4$ nanoparticles were further analyzed using STEM microscopy. STEM micrographs for samples with $x = 1$ and $x = 0.3$ are shown in Figure 2a-b, while the corresponding histograms of the nanoparticle size distribution (*d*: diameter) are displayed in Figures 3c-d. Most of the $Co_xZn_{1-x}Fe_2O_4$ nanoparticles are spherical except $CoFe_2O_4$, which are faceted (see figure 2a). The STEM analysis confirms the previous X-ray characterization, that is, an increasing trend in the mean nanoparticle size as Co content (x) increases.

A slight increase in the mean d value is obtained from STEM micrographs in comparison with those values estimated from the X-ray Rietveld analysis (see Table I). These differences can be attributed to the fact that the STEM sizes are measured within the visible grain limits, while the X-ray estimations are correlated with the crystalline domain. Furthermore, a lognormal distribution properly describes the size distribution of the calcined nanoparticles (see solid line in Figures 2c-d). This type of distribution~~s~~ is usually found in nanoparticle co-precipitated systems and interpreted as a consequence of the synthesis and the grain growth mechanisms [28, 36].

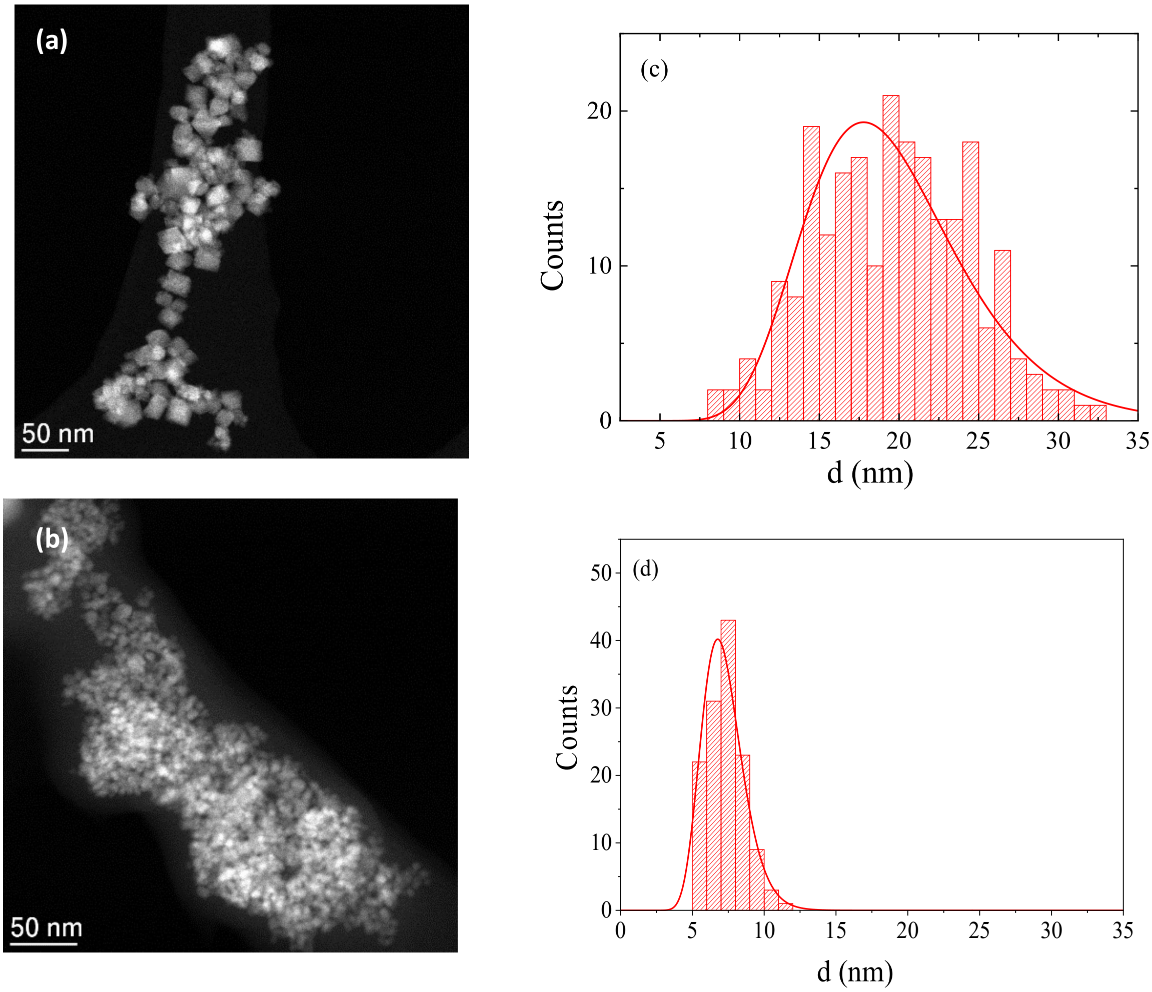

Figure 2. (a) and (b) TEM images and of $Co_xZn_{1-x}Fe_2O_4$ nanoparticles $x = 1$, $x = 0.3$, respectively; (c) $x = 1$ and (d) $x = 3$ nanoparticle size (*d*: diameter) distribution.

The surface area (*BET*) of the nanoparticles represents an important parameter controlling the absorption capacity and thus the photocatalytic activity of the nanophotocatalysts [37]. Generally, a higher surface area promotes a higher photocatalytic efficiency as a consequence of the enhancement of the substrate adsorption on the photocatalyst surface prior to the activation of the photocatalytic reactions.

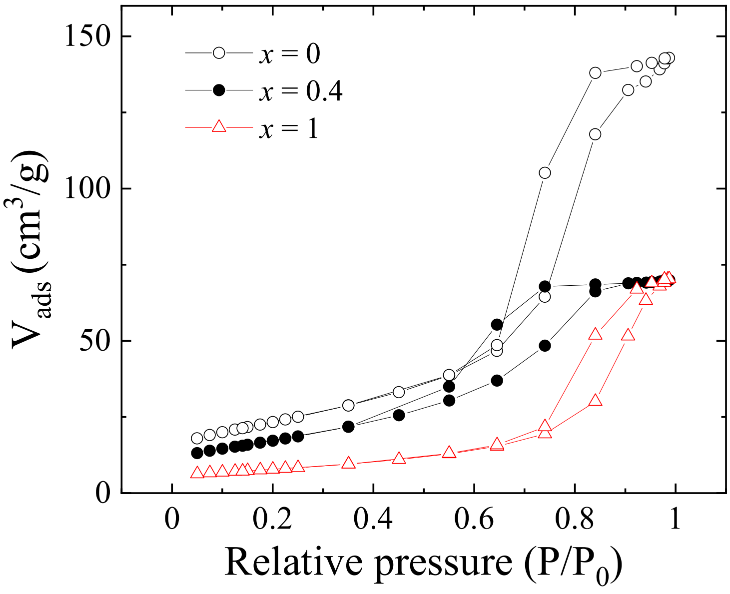

Figure 3. Nitrogen adsorption-desorption curves at 77 K for $Co_xZn_{1-x}Fe_2O_4$ nanoparticles.

As examples, the adsorption-desorption curves of nitrogen at 77 K for some selected compositions (x = 0, 0.4 and 1) are shown in Figure 3. All the nanoparticles display the typical hysteretic curve type V (without initial knee ascribed to the formation of adsorption monolayer), according IUPAC classification [38]. Table II summarizes the estimated *BET* surfaces areas and the pore distribution for the analyzed $Co_xZn_{1-x}Fe_2O_4$ nanoparticles. The samples display *BET* surfaces areas within 60-120 m^2/g and a mesoporous pore distribution (values ranging from 5.8 to 15.8 nm). It is important to remark that no clear trend with x is detected in either *BET* surface or pore diameter.

Table II: *BET* surface, pore diameter and optical band-gaps for $Co_xZn_{1-x}Fe_2O_4$ nanoparticles.

Sample	***BET surface (m²/g)***	***Pore diameter (nm)***	***Indirect Band Gap (eV)***	***Direct Band Gap (eV)***
$x = 0$	83.4	10.6	1.75 ± 0.01	2.97 ± 0.03
$x = 0.1$	92.5	8.5	1.75 ± 0.01	3.03 ± 0.06
$x = 0.3$	103.9	6.1	1.55 ± 0.01	2.91 ± 0.05
$x = 0.4$	66.5	6.7	1.41 ± 0.02	3.13 ± 0.05
$x = 0.5$	79.8	6.0	1.75 ± 0.01	2.97 ± 0.03
$x = 0.6$	82.2	7.8	1.41 ± 0.01	2.96 ± 0.05
$x = 0.7$	100.1	5.8	1.43 ± 0.01	2.93 ± 0.06
$x = 0.9$	124.1	8.5	1.44 ± 0.01	2.99 ± 0.05
$x = 1$	68.1	15.8	1.46 ± 0.02	2.91 ± 0.04

3.2 Optical characterization

The bandgap of the semiconductors plays a dominant role in the photodegradation of organic contaminants due to the generation of electron/hole pairs as a result of the absorption of electromagnetic radiation. Thus, the activation of the photocatalyst in the visible range (wavelength $\lambda > 400$ nm) requires a narrow bandgap photocatalyst with bandgap energy, E_g, below 3 eV.

To estimate the bandgap energy of the calcined Co-Zn ferrites, Diffuse Reflectance Spectroscopy (*DRS*) measurements were carried out. The Kubelka-Munk function, *F(R)*, was employed to determine the optical absorption of the sample through the diffuse reflectance, *R*, $F(R) = \frac{(1-R)^2}{2R}$. Figure 4 shows *F(R)* for the indicated nanoparticles. As Co content increases, the optical absorption shifts towards the visible range (see inset of Figure 4). Similar results, that is, the reduction of the band gap energy in Co-rich Co-Zn ferrites, have been previously reported in Co-Zn ferrites [19, 35, 39, 40].

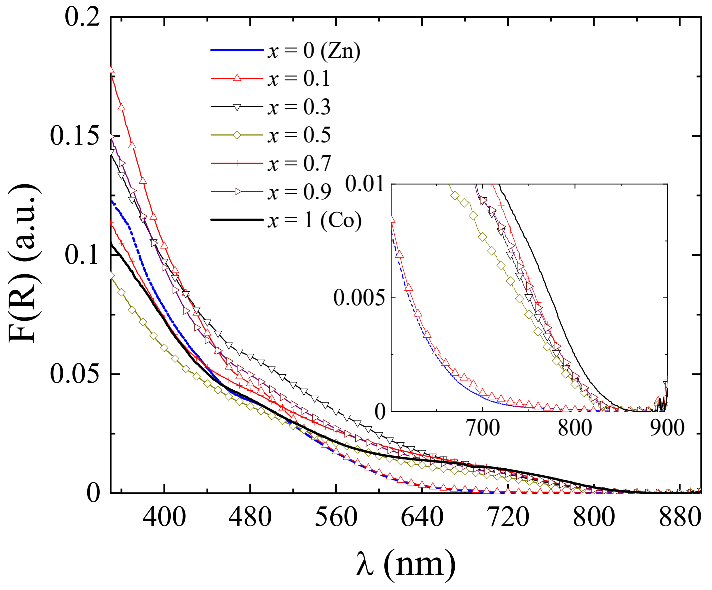

Figure 4. UV-Vis absorption curves obtained from the Diffusive Reflectance Spectroscopy (DRS) for some selected $Co_xZn_{1-x}Fe_2O_4$ nanoparticles.

Since *F(R)* is proportional to the absorption coefficient, the band gap energy can be calculated through the Tauc plot: $(F(R)h\nu)^{\alpha} = (h\nu - E_g)^2$, where $\alpha = ½$ and 2 for direct and indirect transitions, respectively.

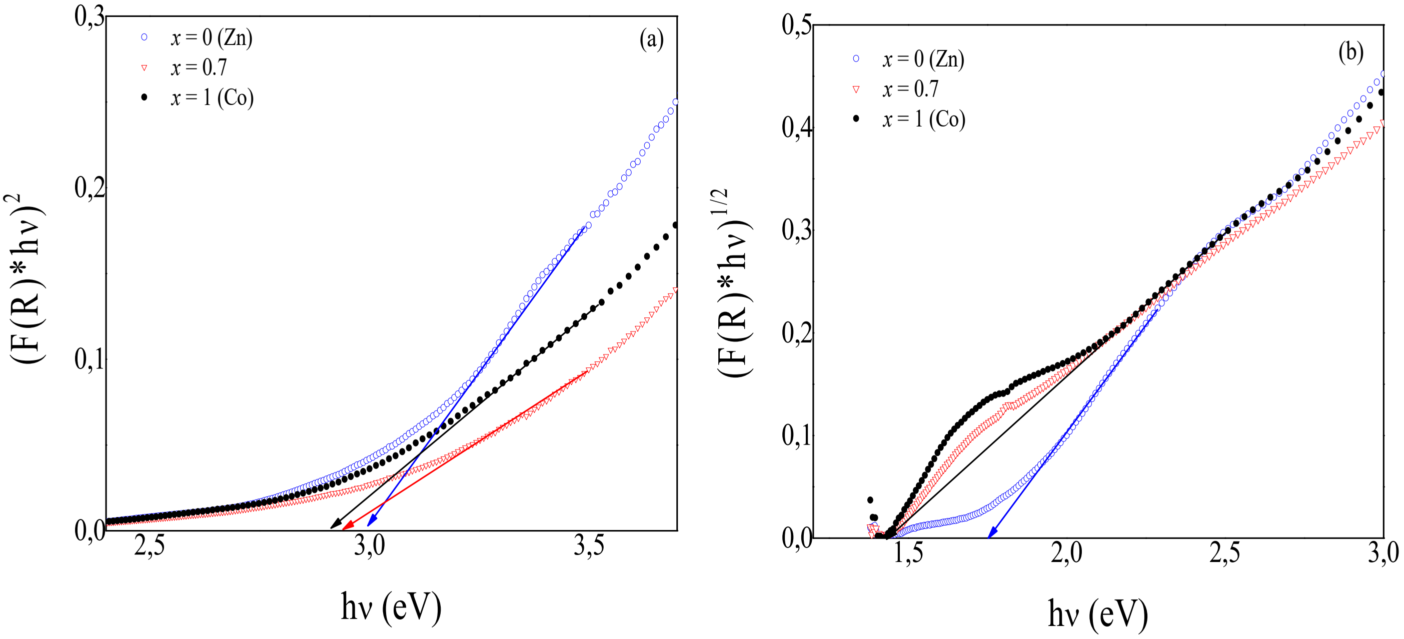

Figure 5. Tauc plots of (a) direct and (b) indirect bandgap for some selected $Co_xZn_{1-x}Fe_2O_4$ nanoparticles.

As examples, Figure 5 shows the obtained Tauc plots for $x = 0$, 0.7 and 1, for (a) direct and (b) indirect transitions. The bandgap values are obtained by extrapolating the linear regions of these plots ($h\nu \rightarrow 0$). The results, both direct and indirect band gaps energies, are resumed in Table II. As previously outlined, it can be concluded that all the synthesized Co-Zn ferrites present E_g values in the range of the visible light (≤ 3 eV). Particularly, a decreasing trend in indirect E_g with x is found. A similar behaviour is found in Co-Zn nanoparticles [19, 35, 39, 40], although the reported values (both direct and indirect band-gaps) show a wide variability linked, among other factors, to the effect of the inversion degree in the band gaps structures [29, 30].

Furthermore, photoluminescence spectroscopy, *PL*, can be used to obtain information about the lifetime of the excited and defect states. A decrease in *PL* intensity is usually ascribed to a reduction in the recombination of the photogenerated electron-hole pairs. Figure 6a shows the *PL* spectrum of some selected Co-Zn ferrites, recorded at the excitation wavelength of 250 nm and room temperature. Three clear emission peaks are detected at $\lambda \approx 400$ nm (violet), 490 nm (green) and 600 nm (yellow) (3.1, 2.5 and 2 eV, respectively). The adscription of these peaks is rather controversial and they are correlated to different emission peaks in the literature [41, 42]. These contradictory results are again linked to the influence of the inversion degree in the band-gap structures [42] and the difficulties to control the cation distribution in the spinel structure through the synthesis procedure. Anyway, the *PL* curves were carefully analyzed through the peak deconvolution employing a Gaussian distribution. Figure 6b shows, the deconvolution obtained for the *PL* curve for $x = 0.6$.

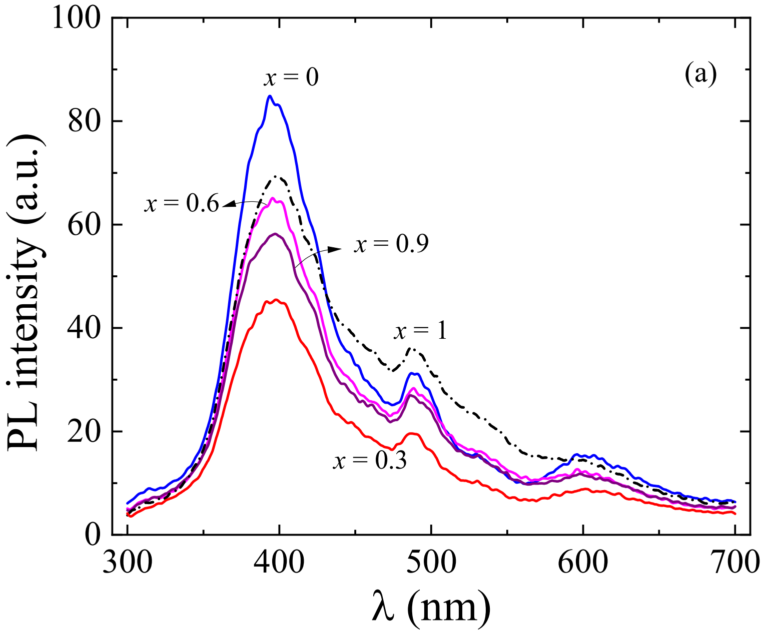

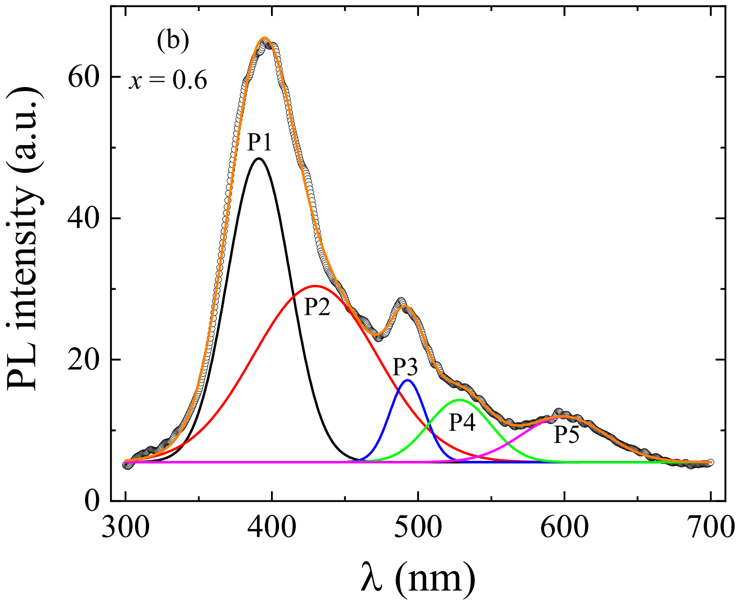

Figure 6. Photoluminescence spectra for $Co_xZn_{1-x}Fe_2O_4$: (a) $x = 0, 0.3, 0.6, 0.9, 1$; (b) deconvoluted *PL* peaks for $x = 0.6$. Inset: Peak amplitudes as a function of x.

Five peaks (*P1*-*P5*) can be detected in all the samples. Firstly, regarding the peak positions, λ_P, the following mean values were obtained: $\lambda_{P1} = 392.6\pm0.4$ nm, $\lambda_{P2} = 440\pm4$

nm, λ_{P3} = 492.1±0.3 nm, λ_{P4} = 525±1 nm, λ_{P5} = 602±1 nm. No remarkable variations in λ_P values were found with the Co content (x), except a slight diminution in *P5* position, varying λ_{P5} from 604.6 to 592.1 nm for $x = 0$ and $x = 1$, respectively. This decrease is in good agreement with the diminution on the indirect band-gap with the Co content (x) of the samples. Regarding the *PL* peak intensity, not conclusive differences are obtained with x. Thus, it cannot be concluded form the *PL* analysis the occurrence of significant differences in the radiative recombination of the electron-hole pairs with x that could affect the photocatalytic performance of the samples.

3.3. Magnetic characterization

As previously outlined, the net magnetic moment in these spinel ferrites is determined by the cation distribution (Zn^{2+}, $Co^{2+}$and Fe^{3+}) between the octahedral and tetrahedral sites. The particular inversion degree depends on different experimental factors such as synthesis procedure, thermal treatments, and mean grain sizes. A maximum value in the net magnetic moment and the saturation magnetization is reported in these Co-Zn ferrites for intermediate compositions (i.e., $0.3 \leq x \leq 0.7$) [27, 28, 43]. Such behavior can also be concluded from Figure 7a, where the high field magnetization, M_{6T}, (applied field $\mu_0 H = 6$ T) is plotted versus temperature, T, (5 K – 300 K) for some selected compositions. Maximum high field magnetization is achieved at 5 K for the samples with $x = 0.6$. However, as previously reported [28], Zn-rich compositions show a certain degree of magnetic frustration at low temperatures. In particular, high field *M(T)* curves departure from the characteristic Bloch's law (continuous decay with T), displaying a peak (maximum value) at a certain temperature. In fact, this behavior in M_{6T} is clearly visible for $x = 0$ (Zn ferrite), displaying a peak in the magnetization around 30

K. As Zn decreases (increase in *x*) the maximum shifts towards lower temperatures, almost vanishing for $x \leq 0.7$ in the analyzed measuring range ($T \geq 5$ K).

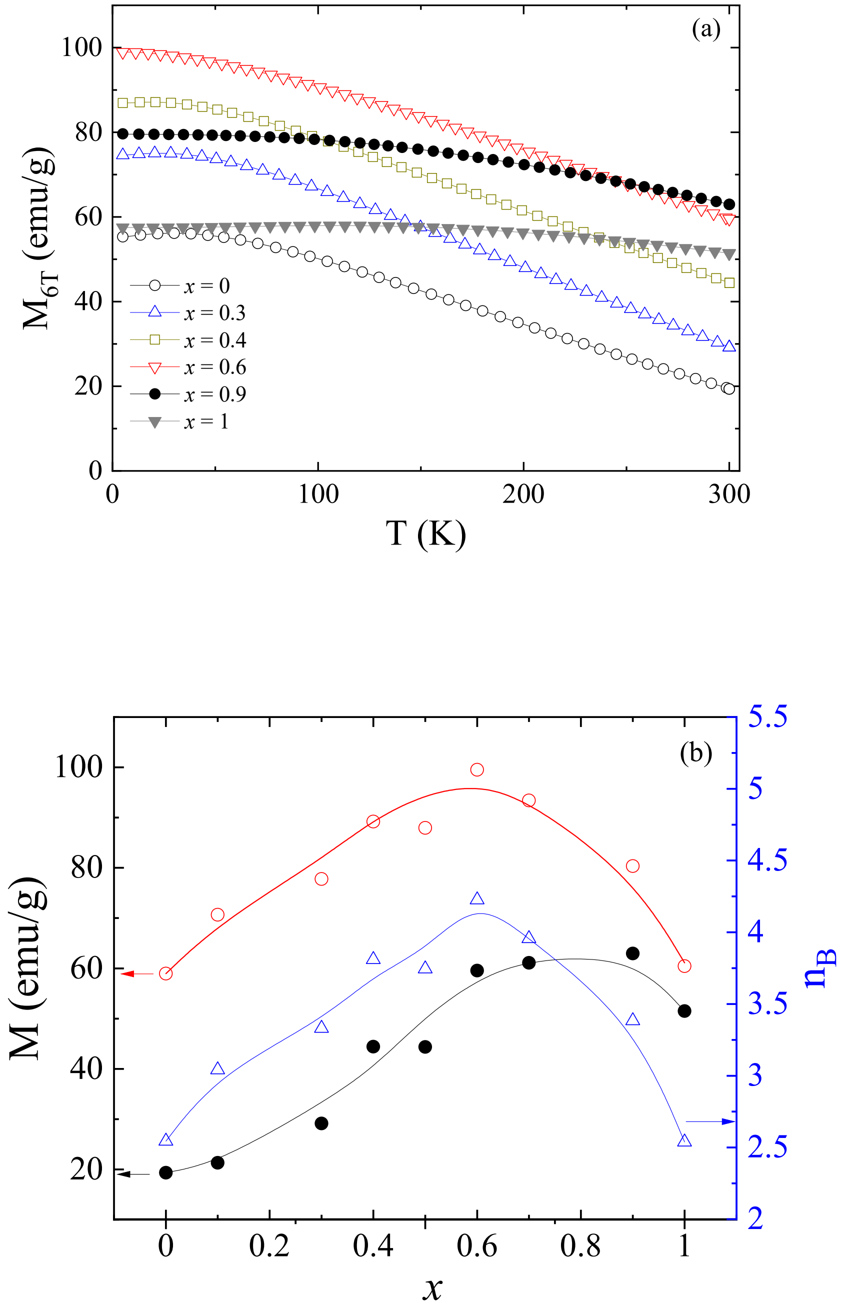

Figure 7: (a) Temperature dependence of the high field magnetization (M_{6T}) for the $Co_xZn_{1-x}Fe_2O_4$ nanoparticles ($\mu_0 H = 6$ T); (b) (○) saturation magnetization, M_0, obtained from the Bloch's law; (△) the number of Bohr magnetons, n_B, per formula unit and (●) the experimental high field magnetization ($\mu_0 H = 6$ T) at 300 K.

Thus, to estimate the effective saturation magnetization, the high field magnetization was fitted in the low temperature range (50 K < T < 150 K) to the Bloch's law: $M_{6T} = M_0 \, (1 - BT^n)$, with M_0 the magnetization at 0 K, B the Bloch constant and n a parameter which value depends on the size of the particles. For $x \leq 0.7$ the best fitting is obtained for $n = 3/2$ (bulk value), while a slight increase in n (≈ 2, typical of nanometric systems) should be considered for Co rich samples. Regarding the Bloch constant, an almost linear decrease is found with x, ranging B between 1.5×10^{-4} K^{-1} to 0.7×10^{-4} K^{-1} for $x = 0$ and $x = 0.7$, respectively. Similar range of values (10^{-4} - 10^{-6}) are reported in different spinel ferrite nanoparticles [42, 44]. A further increase in the Co content ($x \geq 0.9$) promotes a sharp decrease in B (≈ 10^{-7}) clearly visible through the smoother decrease in the magnetization versus T (see Figure 7a). Figure 7b shows the estimated M_0 as a function of the Co content in the nanoparticles together with the number of Bohr magnetons, n_B, per formula unit ($n_B = \frac{M_0 \, M_W}{5585}$; M_W: molecular weight). The results confirm the previously outlined conclusions, that is, maximum M_0 and n_B values for $x = 0.6$. Furthermore, the marked decrease in B for Co-rich spinels ($x \geq 0.7$) leads to maximum high field magnetization values at 300 K for $x \geq 0.6$.

With respect to the low field magnetization, the samples show for $x \leq 0.5$ the characteristic curves of an assembly of superparamagnetic nanoparticles with blocking temperature, T_B, below 300 K (i.e. peak in the *Zero-Field-Cooled* (*ZFC*) magnetization curves around T_B and anhysteretic *M-H* hysteresis loops for $T > T_B$, see Figures 8a and 8b, respectively). As Figure 8a shows, where the *ZFC-FC* magnetization curves (applied magnetic field = 50 Oe) are plotted for $x \leq 0.6$, a general increase in the effective T_B with the Co content (x) can be deduced. Despite T_B is controlled by different parameters (magnetocrystalline anisotropy, nanoparticle interactions or nanoparticle size distribution), its increasing trend with *x* should be ascribed to the increase in the nanoparticle volume (increase in *d*, see Table I).

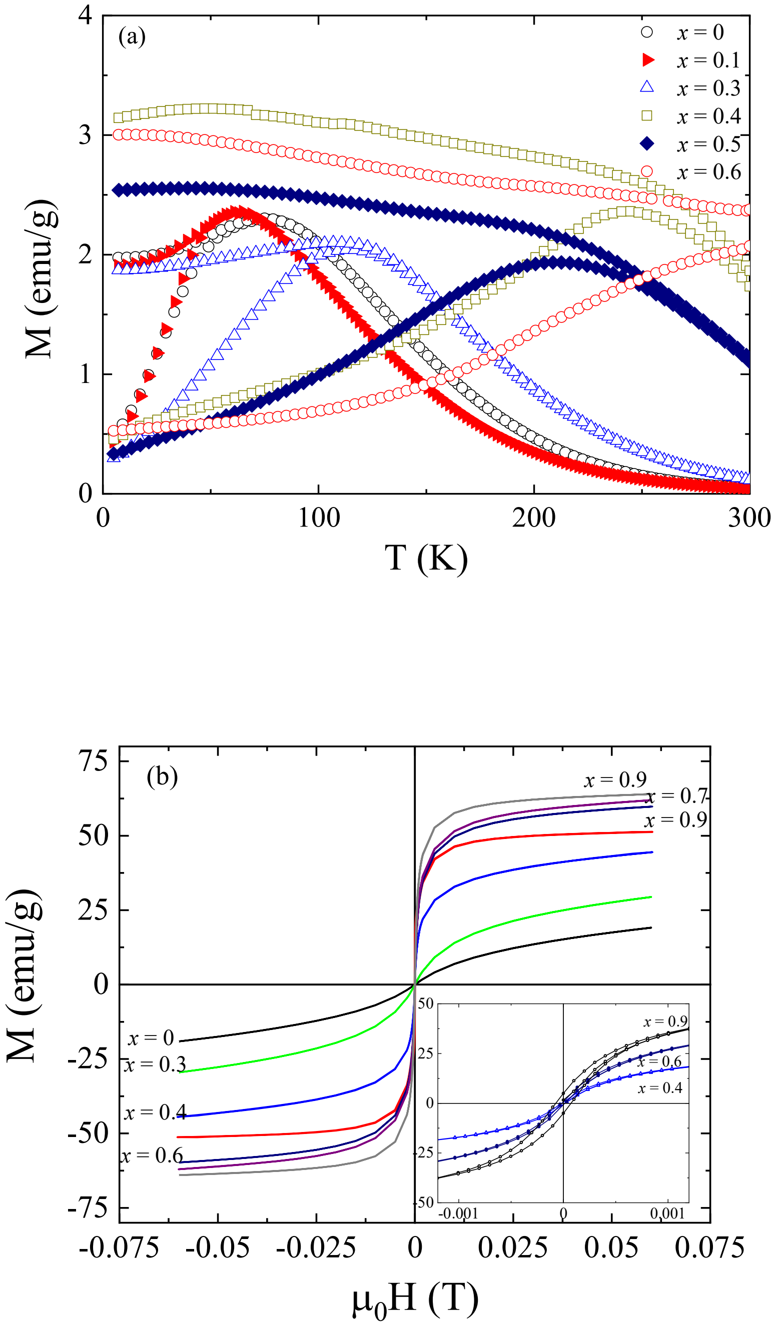

Figure 8: (a) *ZFC-FC* magnetization curves (50 Oe and (b) Room temperature hysteresis loops for the indicated $Co_xZn_{1-x}Fe_2O_4$ nanoparticles. Inset: enlargement of the low field region.

Note that the superparamagnetic behavior at 300 K can be further checked through the occurrence of anhysteretic *M-H* hysteresis loops (see Figure 8b). As the inset of this

Figure shows, negligible remanence and coercive field are found for nanoparticles $x < 0.6$. The superparamagnetic behavior is of relevance considering the photocatalytic applications, enabling a better dispersion of the nanoparticles in the absence of an external applied magnetic field. Additionally, the increase in x (increase in Co content) leads to a parallel increase in the initial magnetic susceptibility ($H \rightarrow 0$) at 300 K correlated to the increase in the saturation magnetization. Thus, the application of an external magnetic field would enable an efficient magnetic separation as a result of the high magnetic susceptibility of these superparamagnetic entities.

3.4 Photocatalytic activity

Prior to the photocatalytic characterization, the nanoparticles' stability in aqueous dispersion was analyzed through the analysis of the electrostatic charge of the nanoparticles. Particularly, the nanoparticles' Zeta potential was characterized as a function of the pH of the medium. The isoelectric point (*IEP*) is defined as the pH at which the Zeta potential achieves a net value of zero. Thus, higher pH values give rise to a negative surface charge, while lower pH values than *IEP* lead to a positive surface charge. The nanoparticles display a similar behavior, with a mean value $IEP = 4.2 \pm 0.1$. Therefore, it can be concluded that for acidic conditions, nanoparticles are positively charged, while for $\text{pH} \geq 4$ they display a negative electrostatic charge. Since the photocatalytic experiments were performed at pH neutral (pH = 7), a negative charge should be assumed on the nanoparticle surface. As a weak acid with pKa equal to 10, phenol was present in the solution with a pH of 7, mainly in the molecular form, and the suspensions of all tested particles were stable and did not agglomerate during the photocatalytic reaction. Moreover, due to the similarity between *IEP* of the nanoparticles, no remarkable variations should be expected in the interparticle interactions (dispersion) or substrate adsorption (i.e., phenol) between the different compositions correlated to their electrostatic charge.

Focusing on the photocatalytic response, phenol photodegradation was firstly investigated employing the Co-Zn nanoparticles under the same reaction conditions. First, the changes in the phenol concentration (% *phenol* = $\left(\frac{C_0-C_f}{C_0}\right) \times 100;$ C_f and C_0 are the final and initial phenol concentrations, respectively, measured through HPLC, were evaluated under dark for 2 hours. The results show a decrease in C_f that should be ascribed to the phenol adsorption on the photocatalysts surface under dark (see solid bars in Figure 9a). Particularly, maximum adsorption (around 25 %) is found in the Co ferrite ($CoFe_2O_4$) that, according to the previous physicochemical characterization, could be correlated with its largest pore diameter (see Table II). However, enhanced dark adsorption is also found for $x = 0.4$ and $x = 0.5$ nanoparticles (20 and 15%, respectively) that cannot be ascribed to any of the previously analyzed physicochemical parameters. Hereafter, similar experiments were performed under visible light radiation (Xenon lamp with 400 nm cut-off filter) for 2 hours (Figure 9a, striped bars). As the content of cobalt increases, % *phenol* raises up to a maximum (% *phenol* ≈ 30% for $0.4 \leq x \leq 0.6$) with the following decay for $x \geq 0.7$. Surprisingly, these samples also display maximum values of the saturation magnetization and net magnetic moment (see Figure 7b).

In order to compare the optimization of the photocatalytic performance for these intermediate compositions, $Co_xZn_{1-x}Fe_2O_4$ nanoparticles with $x = 0.1$, 0.4, 0.6 and 0.9 were tested for gas phase toluene degradation. A similar procedure (comparison under dark and under irradiation) was performed. The toluene degradation was analyzed through % *toluene* = $\left(\frac{C_0-C_f}{C_0}\right) \times 100,$ with C_f and C_0 the final and initial toluene concentrations, respectively, measured through a gas chromatograph. In this case, light irradiation (LEDs) with 415 nm was employed during different times until the toluene concentration remained stable.

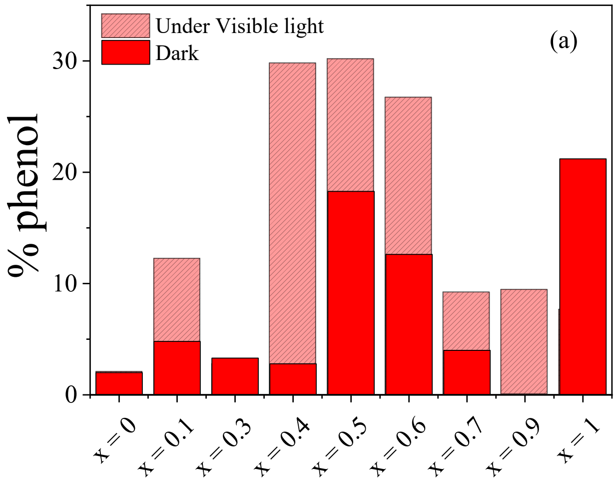

Figure 9. (a) Phenol photodegradation (% *phenol)* and (b) iToluene photodegradation *(% toluene*) n the presence of $Co_xZn_{1-x}Fe_2O_4$ nanoparticles under dark (solid bars) and under radiation (striped bars).

Figure 9b compares the maximum % *toluene* in dark conditions (solid bars) versus irradiation striped bars). Again, maximum toluene photocatalytic degradation (under irradiation) is achieved for $0.4 \leq x \leq 0.6$ nanoparticles.

5. Discussion

Firstly, regarding the proposed photocatalytic applications, it can be concluded that those compositions with $0.4 \leq x \leq 0.6$ display optimum magnetic response, that is, superparamagnetic behavior at 300 K that reduces nanoparticle aggregation and high net magnetic moment to ensure an efficient magnetic separation. Furthermore, these samples are characterized by maximum degradation both for phenol and toluene (see Figure 9).

Thus, the simultaneous optimization on the magnetic and photocatalytic response provides relevant characteristics to these spinel ferrites, not only from an applied perspective but also in the analysis of the intrinsic factors that control the photocatalytic response.

Previous works in Co-Zn nanoparticles also report the occurrence of enhanced photocatalytic degradation for intermediate (mixed) compositions, but the main origin is ascribed to different physicochemical parameters without a common conclusive discussion [32, 33, 35, 45, 46]. In fact, within the present study, none of the analyzed physicochemical parameters (with the exception of the net magnetic moment and saturation magnetization) could explain the detected enhancement of the photocatalytic performance for the particular compositional range ($0.4 \leq x \leq 0.6$). Neither the lattice parameter, mean nanoparticle size, *BET* surface area and pore diameter, energy bandgap, photoluminescence (*PL*) response or *IEP* display an evolution with the nanoparticle composition that could justify the detected enhanced the photocatalytic degradation for intermediate values of x. Notice that, even the employ of different substrates (phenol or toluene), different irradiation conditions (Xenon lamp with 400 nm cut-off filter or 415 nm LED) and experimental configuration (aqueous solution or gaseous phase) do not alter the above conclusion. Although the reduction of the bandgap energy for Co rich nanoparticles would explain the improvement of the photocatalytic performance within the visible range, it could not justify the observed optimization for intermediate Co-Zn compositions and the decrease of the maximum pollutant degradation for Co rich nanoparticles. However, the net magnetic moment of the spinel ferrites clearly shows maximum values within this optimum photocatalytic response range. Therefore, the crucial point is to analyze whether the net magnetic moment or the saturation magnetization of the photocatalyst could have associated an intrinsic enhancement in the photocatalytic response.

As previously outlined (see Introduction), the application of external magnetic fields (B) has been previously reported as an effective strategy to enhance the photocatalytic performance [8-16]. When B is applied to paramagnetic or diamagnetic photocatalysts, both contributions of the Lorentz forces and the Magnetohydrodynamic (*MHD*) effects should be taken into consideration. In the case of Lorentz forces ($F_L \propto qvB$, being q and v the charge and velocity of the charged species, respectively), magnetic field modifies the dispersion and distribution of chemical radicals (i.e. OH^-). Additionally, these magnetic forces can also suppress the carrier recombination as a consequence of the charge (electron-hole) separation [47, 48]. With respect to the *MHD* effects, the magnetic forces mainly act on paramagnetic species and molecules (i.e. dissolved oxygen) due to the occurrence of magnetic field gradients in the media ($F_L \propto \chi B \nabla B$) [11]. Both Lorentz and MHD forces not only affect the photocatalytic reactions but also control the adsorption processes on the catalyst surface. Furthermore, the occurrence of spin selectivity effect between the spin of the radicals (i.e. $^{\bullet}OH$) and the catalysts is also proposed as a controlling factor on the photocatalytic reactions. In fact, spin polarization is proposed as the key factor controlling the magnetic field enhancement in defective TiO_2 based photocatalysts [15, 16] and spinel Zn ferrite [49]. However, the radial-pair mechanism is also invoked as the main origin of the enhancement on the photocatalytic performance under moderate magnetic field strengths [11, 50, 51]. These models, included within the *spin chemistry*, are based on the fundamental principle of the conservation of the total spin in chemical reactions [52]. Thus, a radical pair, formed due to bond breaking by photoexcitation or by charge transfer with donor or acceptors, is a short-lived reaction intermediate comprising two radicals formed in tandem that can exist in a singlet (*S*) or triplet (*T*) states. Recombination to form the diamagnetic zero spin molecule takes place from the reactive *S* state, while spin changing to the nonreactive triplet state would lead to a reduction in the recombination radical pair rate. Different factors could modify $S \leftrightarrow T$ radical pair conversion (hyperfine coupling, spin-orbit interaction, interaction with microwaves, exchange interaction with a third spin carrier).In fact, the application of external magnetic fields would modify the singlet-triplet conversion, leading to stable triplet pairs able to interacting with the organic pollutants.

However, photocatalysis is a very complex process involving different factors governing the degradation of the organic molecules, where the generation of free active radicals can be considered as the last stage of the process. However, irrespectively of the actual mechanism responsible of the magnetic field effect, its contribution is unquestionable in view of the latest reported results [8-16, 49-51]. The present study clearly shows a link between the enhanced photocatalytic degradation and the increase in the net magnetic moment of the nanophotocatalysts. In fact, similar enhancements in the (photo)catalytic and electrocatalytic response with the catalyst magnetization can be found in the literature, although its correlation with the net magnetic moment (saturation magnetization) is not directly stated [53-56]. Whether the analyzed photocatalytic enhancement in these Co-Zn is related to the “effective” magnetic field associated with their intrinsic magnetization, interacting with the chemical species involved in the photocatalytic processes, or to the spin polarization state of the photoexcited electron-holes in the semiconductor photocatalysts, is open for discussion. Anyway, the present results supports a new research strategy in developing highly efficient photocatalytic materials, where the intrinsic magnetic contribution associated to the ferri or ferromagnetic nature of photocatalysts would play an outstanding role.

4. Conclusions

The photocatalytic performance of Co-Zn spinel ferrite nanoparticles has been analyzed, focusing on the correlation with their magnetic response. $Co_xZn_{1-x}Fe_2O_4$ nanoparticles, obtained by the co-precipitation method, show mean grain sizes and lattice parameters that inversely evolve with the Co concentration (increase and decrease, respectively). The nanometric size gives rise to superparamagnetism at room temperature that prevents nanoparticle aggregation and enhances the nanoparticle's stability in aqueous media. Furthermore, due to the mixed inversion character of the spinel ferrites, a maximum value of the net magnetic moment (saturation magnetization) is found for $0.4 \leq x \leq 0.6$. Remarkable maximum degradation efficiencies under visible irradiation for both phenol and toluene are found in the same compositional range. This behavior cannot be explained, considering the comparative analysis of characteristic physicochemical parameters (specific surface area, isoelectric point, bandgap energy, photoluminescence). Thus, the effect of the intrinsic magnetic contribution linked to the magnetization of the nanoparticles is proposed as the main origin of photocatalytic enhancement.

Acknowledgements.

The work has been performed under grant PID2020-116321RB-C21 funded by MCIN/AEI/ 10.13039/501100011033. Authors would like to acknowledge the use of *Servicio General de Apoyo a la Investigación-SAI*, Universidad de Zaragoza for the microscopy and X-Ray fluorescence analysis. Diffuse Reflectance Spectroscopy analyses were carried out in the Chemical Synthesis and Homogeneous Catalysis Institute (ISQCH) Universidad de Zaragoza-CSIC. (Dr. Eugenio Vispe). L. Cervera-Gabalda acknowledges Public University of Navarre for her Ph.D contract "Contratos Predoctorales adscritos a Grupos e Institutos de Investigación de la Universidad Pública de Navarra" and Government of Navarre “Ayudas al Plan de Formación y de Investigación y Desarrollo (I+D)” for the pre-doctoral research stay support at the Department of Process Engineering and Chemical Technology at Gdansk University of Technology. AZJ acknowledges the Polish National Science Centre (grant no. NCN 2018/30/E/ST5/00845).

References

1.WORLD HEALTH ORGANIZATION, et al. *Progress on household drinking water, sanitation and hygiene 2000-2020: five years into the SDGs*. 2021. ISBN (WHO) 978-92-4-003084-8.

2. S.H.S. Chan, T. Yeong Wu, J.C. Juan. and C.Y. Teh, *Recent developments of metal oxide semiconductors as photocatalysts in advanced oxidation processes (AOPs) for treatment of dye waste-water*. J. Chem. Technol. Biotechnol., 86 (2011) 1130-1158. https://doi.org/10.1002/jctb.2636.

3. H. Liu, C. Wang, G. Wang, *Photocatalytic Advanced Oxidation Processes for Water Treatment: Recent Advances and Perspective*, Chem. Asian J. 15 (2020) 3239. https://doi.org/10.1002/asia.202000895.

4. S. Rehman, R. Ullah, A.M. Butt, N.D. Gohar, *Strategies of making* TiO_2 *and ZnO visible light active*, J. Hazard. Mater., 170, 2–3 (2009) 560-569. https://doi.org/10.1016/j.jhazmat.2009.05.064.

5. F. Deng, H. Shi, Y. Guo, X. Luo, J. Zhou, *Engineering paths of sustainable and green photocatalytic degradation technology for pharmaceuticals and organic contaminants of emerging concern*, Curr. Opin. Green Sustain. Chem., 29 (2021) 100465. https://doi.org/10.1016/j.cogsc.2021.100465.

6. K. Bisaria, S. Sinha, R. Singh, Hafiz M.N. Iqbal, *Recent advances in structural modifications of photo-catalysts for organic pollutants degradation – A comprehensive review*, Chemosphere, 284 (2021) 131263. https://doi.org/10.1016/j.chemosphere.2021.131263.

7. C. Hu, S. Tu, N. Tian, T. Ma, Y. Zhang, H. Huang, *Photocatalysis Enhanced by External Fields*, Angew. Chem. Int., 133 (2021) 16309–16328. doi.org/10.1002/anie.20200951.

8. L. Shi, X. Wang, Y. Hu, Y. He, *Investigation of photocatalytic activity through photo-thermal heating enabled by* Fe_3O_4/TiO_2 *composite under magnetic field,* Sol. Energy 196 (2020) 505-512. https://doi.org/10.1016/j.solener.2019.12.053.

9. N. Li, M. He, X. Lu, L. Liang , R. Li, B. Yan, G. Chen, *Enhanced norfloxacin degradation by visible-light-driven* Mn_3O_4*/γ-MnOOH photocatalysis under weak magnetic field*, Sci. Total Environ. 761 (2021) 143268. https://doi.org/10.1016/j.scitotenv.2020.143268.

10. W. Gao, X.L. Zhao, C. Cui, X. Su et al. *High-efficiency separation and transfer of photo-induced charge carrier in graphene/*TiO_2 *via heterostructure in magnetic field*, J. Alloy. Compd. 862 (2021) 158283. https://doi.org/10.1016/j.jallcom.2020.158283.

11. H. Okumura, S. Endo, S. Joonwichien, E. Yamasue, K.N. Ishihara, *Magnetic field effect on heterogeneous photocatalysis*, Catal. Today 258, 2 (2015) 634-647. https://doi.org/10.1016/j.cattod.2014.12.048.

12. C. Peng, W. Fan, Q. Li, W. Han, X. Chen, G. Zhang, Y. Yan, Q. Gu, C. Wang, H. Zhang, P. Zhang, *Boosting photocatalytic activity through tuning electron spin states and external magnetic fields*, J Mater Sci Technol. 115 (2022) 208-220. https://doi.org/10.1016/j.jmst.2021.11.031.

13. Y. Pan, Q. Wang, M. Zhou, J. Cai, Y. Tian, Y. Zhang, *Kinetic and mechanism study of UV/pre-magnetized-*Fe^0*/oxalate for removing sulfamethazine*, J. Hazard. Mater., 398 (2020) 122931. https://doi.org/10.1016/j.jhazmat.2020.122931.

14. Y. Lu, B. Ren, S. Chang, W. Mi, J. He, W. Wang, *Achieving effective control of the photocatalytic performance for* $CoFe_2O_4$/MoS_2 *heterojunction via exerting external magnetic fields*, Mater. Lett. 260 (2020) 126979. https://doi.org/10.1016/j.matlet.2019.126979.

15. L. Pan, M. Ai, M., C. Huang, et al. *Manipulating spin polarization of titanium dioxide for efficient photocatalysis.* Nat Commun 11, 418 (2020). https://doi.org/10.1038/s41467-020-14333-w.

16. Y. Li, Z. Wang, Y. Wang, A. Kovács, C. Foo, R. E. Dunin-Borkowski, Y. Lu, R. A. Taylor, C. Wu, S. C. Edman Tsang, *Local Magnetic Spin Mismatch Promoting Photocatalytic Overall Water Splitting with Exceptional Solar-to-Hydrogen Efficiency.* Energy Environ. Sci., 15 (2022) 265-277. https://doi.org/10.1039/D1EE02222A.

17. K.K. Kefeni, B.B. Mamba, T.A.M. Msagati *Application of spinel ferrite nanoparticles in water and wastewater treatment: A review, Sep. Purif. Technol.* 188 (2017) 399 – 422. https://doi.org/10.1016/j.seppur.2017.07.015.

18. N.K. Gupta, Y. Ghaffari, S. Kim, J. Bae, K. Soo Kim, Md Saifuddin, *Photocatalytic Degradation of Organic Pollutants over* MFe_2O_4 *(M = Co, Ni, Cu, Zn) Nanoparticles at Neutral pH*. Sci Rep 10 (2020)4942. https://doi.org/10.1038/s41598-020-61930-2.

19. A. Sutka, M. Millers, M. Vanags, U. Joost, M. Maiorov, V. Kisand, R. Pa¨rna, I. Juhnevica, *Comparison of photocatalytic activity for different co-precipitated spinel ferrites,* Res Chem Intermed 41(2015) 9439–9449. DOI 10.1007/s11164-015-1969-6.

20. K. Jangam, K. Patil, S. Balgude, S. Patange, P. More *Magnetically separable* $Zn_{1-x}Co_{0.5x}Mg_{0.5x}Fe_2O_4$ *ferrites: stable and efficient sunlight-driven photocatalyst for*

environmental remediation, RSC Adv. 10 (2020) 42766-42776. DOI: 10.1039/D0RA08172H.

21. M. Su, C. He, V. K.Sharma, M. Abou Asi, D. Xia, X.-Z. Li, H. Deng, Y. Xiong, *Mesoporous zinc ferrite: Synthesis, characterization, and photocatalytic activity with H_2O_2/visible light*, J. Hazard. Mater. 211–212 (2012) 95-103. https://doi.org/10.1016/j.jhazmat.2011.10.006.

22. C. Caia, Z. Zhang, J. Liu, N. Shan, H. Zhang, D. Dionysiou, *Visible light-assisted heterogeneous Fenton with $ZnFe_2O_4$ for the degradation of Orange II in water*, Appl. Catal. B-Environ. 182 (2016) 456-468. https://doi.org/10.1016/j.apcatb.2015.09.056.

23. T. Tabari, D. Singh, S. S. Jamali, *Enhanced photocatalytic activity of mesoporous $ZnFe_2O_4$ nanoparticles towards gaseous benzene under visible light irradiation*, J. Environ. Chem. Eng. 5, 1, (2017) 931-939. https://doi.org/10.1016/j.jece.2017.01.016.

24. R. Li, H. Hu, Y. Ma, X. Liu, L. Zhang, S. Zhou, B. Deng, H. Lin, H. Zhang, *Persulfate enhanced photocatalytic degradation of bisphenol A over wasted batteries-derived $ZnFe_2O_4$ under visible light*, J. Clean Prod. 276, 10 (2020) 124246. https://doi.org/10.1016/j.jclepro.2020.124246.

25. B. Antic, M. Perovic, A. Kremenovic, J. Blanusa, V. Spasojevic, P. Vulic, L. Bessais, E.S. Bozin, *An integrated study of thermal treatmenteffects on the microstructure and magnetic properties of Zn–ferritenanoparticles*, J. Phys.: Condens. Matter 25 (2013) 086001. doi:10.1088/0953-8984/25/8/086001.

26. V. Blanco-Gutierrez, E.Climent-Pascual, M.J.Torralvo-Fernandez, R.Saez-Puche, M.T.Fernandez-Diaz, *Neutron diffraction study and superparamagnetic behavior of $ZnFe_2O_4$ nanoparticles obtained with different conditions,* J. Solid State Chem. 184, 7, (2011) 1608-1613. https://doi.org/10.1016/j.jssc.2011.04.034.

27. M. Veverka, Z. Jirak, O. Kaman, K. Knizek, M. Marysko, E. Pollert, K. Zavta, A. Lancok, M. Dlouha, S. Vratislav, *Distribution of cations in nanosize and bulk Co-Zn ferrites,* Nanotechnology, 22 (2011) 345701. https://doi.org/10.1088/0957-4484/22/34/345701.

28. C. Gómez-Polo, V. Recarte, L.Cerver, J.J.Beato-López, J. López-García, J.A. Rodríguez-Velamazán, M.D. Ugarte, E.C. Mendonça, J.G.S. Duque, J. Magn. Magn. Mat. 465, 1 (2018) 211-219. https://doi.org/10.1016/j.jmmm.2018.05.051.

29. K. Dileep, B. Loukya, N. Pachauri, A. Gupta, R. Datta, *Probing optical band gaps at the nanoscale in $NiFe_2O_4$ and $CoFe_2O_4$ epitaxial films by high resolution electron energy loss spectroscopy*, J. Appl. Phys. 116 (2014) 103505. https://doi.org/10.1063/1.4895059.

30. L. I. Granone, A.C. Ulpe, L. Robben, S. Klimke, M. Jahns, F. Renz, T.M. Gesing, T. Bredow, R. Dillert, D.W. Bahnemann, *Effect of the degree of inversion on optical properties of spinel $ZnFe_2O_4$*, Phys. Chem. Chem. Phys.20 (2018) 28267-28278. DOI: 10.1039/C8CP05061A.

31. J. Rodriguez-Carvajal, *Recent advances in magnetic structure determination by neutron powder diffraction.* Physica B, 192 (1993) 55. doi.org/10.1016/0921-4526(93)90108-I.

32. M. Sundararajan, V. Sailaja, L. John Kennedy, J. Judith Vijaya, *Photocatalytic degradation of rhodamine B under visible light using nanostructured zinc doped cobalt ferrite: Kinetics and mechanism*, Ceram. Int. 43, 1, Part A, (2017) 540-548. https://doi.org/10.1016/j.ceramint.2016.09.191.

33. M. Madhukara Naik, H.S. Bhojya Naik, G. Nagaraju, M. Vinuth, K.Vinu, R. Viswanath, *Green synthesis of zinc doped cobalt ferrite nanoparticles: Structural, optical, photocatalytic and antibacterial studies*, Nano-Structures & Nano-Objects 19 (2019) 100322. https://doi.org/10.1016/j.nanoso.2019.100322.

34. M. Ben Ali, K. E lMaalam, H. El Moussaoui, O.Mounkachi, M.Hamedoun, R. Masrour, E.K.Hlil, A.Benyousse, f*Effect of zinc concentration on the structural and magnetic properties of mixed Co–Zn ferrites nanoparticles synthesized by sol/gel method*, J. Magn. Magn. Mat. Volume 398, 15, (2016) 20-25.
https://doi.org/10.1016/j.jmmm.2015.08.097.

35. G. Fan, J. Tong, F. Li, *Visible-Light-Induced Photocatalyst Based on Cobalt-Doped Zinc Ferrite Nanocrystals*, Ind. Eng. Chem. Res. 2012, 51, 42, 13639–13647. https://doi.org/10.1021/ie201933g.

36. V. Mameli, A. Musinu, A. Ardu, G. Ennas, D. Peddis, D. Niznansky, C. Sangregorio, C. Innocenti, Nguyen T. K. Thanh, C. Cannas, *Studying the effect of Zn-substitution on the magnetic and hyperthermic properties of cobalt ferrite nanoparticles*, Nanoscale, 2016, 8, 10124-10137 DOI: 10.1039/C6NR01303A.

37. C. Gomez-Polo, S. Larumbe, A. Gil, D. Muñoz., L. RodríguezFernández, L. Fernández Barquín, A. García-Prieto, M. L. Fdez-Gubieda, A.Muela, *Improved photocatalytic and antibacterial performance of Cr doped* TiO_2 *nanoparticles*, Surf. Interfaces 22 (2021) 100867. https://doi.org/10.1016/j.surfin.2020.100867.

38. M. Thommes, K. Kaneko, A. V. Neimark, J. P. Olivier, F. Rodriguez-Reinoso, J. Rouquerol, Kenneth S. W. Sing, *Physisorption of gases, with special reference to the evaluation of surface area and pore size distribution (IUPAC Technical Report)*, Pure Appl. Chem.; 8, 9-10 (2015) 1051–1069. DOI 10.1515/pac-2014-1117.

39. M. Sundararajan, L. John Kennedy, Udaya Aruldoss, Sk. Khadeer Pasha, J. JudithVijaya, Steve Dunn, *Microwave combustion synthesis of Zinc substituted nanocrystalline spinel cobalt ferrite: Structural and magnetic studies*, Mater. Sci. Semicond. Process 40 (2015) 1-10. https://doi.org/10.1016/j.mssp.2015.06.002.

40. T.R. Tatarchuk, N.D.Paliychuk, M.Bououdinam B.Al-Najar, M.Pacia, W.Macyk, A.Shyichuk, *Effect of cobalt substitution on structural, elastic, magnetic and optical properties of zinc ferrite nanoparticles*, J. Alloy. Compd. 731 (2018) 1256-1266. https://doi.org/10.1016/j.jallcom.2017.10.103.

41. L.I. Granone, K. Nikitin, A. Emeline, R. Dillert, D.W. Bahnemann, *Effect of the Degree of Inversion on the Photoelectrochemical Activity of Spinel* $ZnFe_2O_4$, Catalysts, 9(5) (2019) 434. https://doi.org/10.3390/catal9050434.

42. P.T. Phong, P.H. Nam, N.X. Phuc, et al. *Effect of Zinc Concentration on the Structural, Optical, and Magnetic Properties of Mixed Co-Zn Ferrites Nanoparticles Synthesized by Low-Temperature Hydrothermal Method*. Metall Mater Trans A 50, 1571–1581 (2019). https://doi.org/10.1007/s11661-018-5096-z.

43. G.A. Petit, D.W. Forester, *Mössbauer study of Co-Zn ferrites,* Phys. Rev. B, 4 (1971), 3912-3923. https://doi.org/10.1103/PhysRevB.4.3912.

44. R. Ghasemi, J. Echeverría, J.I. Pérez-Landazábal, J.J. Beato-Lopez, M. Naseri, C. Gómez-Polo, *Effect of Cu substitution on the magnetic and magnetic induction heating response of* $CdFe_2O4$ *spinel ferrite,* J. Man. Magn. Mat. 499, 1 (2020) 166201. https://doi.org/10.1016/j.jmmm.2019.166201.

45. D. Chahar, S. Taneja. S. Bishta, S. Kesarwani, P. Thakur, A. Thakur, P.B. Sharma, *Photocatalytic activity of cobalt substituted zinc ferrite for the degradation of methylene blue dye under visible light irradiation*, J. Alloy. Compd. 851, 15 (2021) 156878. https://doi.org/10.1016/j.jallcom.2020.156878.

46. J. Revathi, M. John Abel, C. Lydia Pearline, T. Sumithra, P. Fermi Hilbert Inbaraj, J. Joseph Prince, *Influence of* Zn^{2+} *in* $CoFe_2O_4$ *nanoparticles on its photocatalytic activity under solar light irradiation*, Inorg. Chem. Commun.121 (2020) 108186. https://doi.org/10.1016/j.inoche.2020.108186.

47. W. Gao, J. Lu, S. Zhang, X. Zhang, Z. Wang, W. Qin, J. Wang, W. Zhou, H. Liu, Y. Sang, *Suppressing Photoinduced Charge Recombination via the Lorentz Force in a Photocatalytic System*, Adv. Sci., 6 (2019) 1901244. https://doi.org/10.1002/advs.201901244.

48 Y. Bian, G. Zheng, W. Ding, L. Hu, Z. Sheng, *Magnetic field effect on the photocatalytic degradation of methyl orange by commercial TiO2 powder*, RSC Adv., 11 (2021) 6284-6291. https://doi.org/10.1039/D0RA08359C.

49. W. Gao, R. Peng, Y. Yang, X. Zhao, C. Cui, X. Su, W. Qin, Y. Dai, Y. Ma, H. Liu, Y. Sang, *Electron Spin Polarization-Enhanced Photoinduced Charge Separation in Ferromagnetic* $ZnFe_2O_4$ ACS Energy Letters 6 (6), (2021) 2129-2137. DOI: 10.1021/acsenergylett.1c00682.
50. H. Dan, Y. Kong, Q. Yue, J. Liu, X. Xu, W. Kong, Y. Gao, B. Gao, *Magnetic field-enhanced radical intensity for accelerating norfloxacin degradation under FeCu/rGO photo-Fenton catalysis*, Chem. Eng. J., 420, 2 (2021) 127634. https://doi.org/10.1016/j.cej.2020.127634.

51. R. Dhanalakshmi, N.V. Giridharan, J.C. Denardin, J.C. *Magnetic Field-Assisted Photocatalytic Degradation of Organic Pollutants over* $Bi_{1-x}R_xFeO_3$ *(R = Ce, Tb; x = 0.00, 0.05, 0.10 and 0.15) Nanostructures.* Materials 14 (2021) 4079. https://doi.org/10.3390/ma14154079.

52. A.L. Buchachenko, V.L. Berdinsky, *Electron Spin Catalysis*, Chem Rev 102 (3), (2002) 603-612. DOI: 10.1021/cr010370l.

53. J.A. Toledo-Antonio, N. Nava, M. Martínez, X. Bokhimi, *Correlation between the magnetism of non-stoichiometric zinc ferrites and their catalytic activity for oxidative dehydrogenation of 1-butene*, Appl. Catal. A-Gen. 234, I1–2, 8 (2002) 137-144. https://doi.org/10.1016/S0926-860X(02)00212-0.

54. J. Ma, C. Liu, K. Chen, *Insight in the relationship between magnetism of stoichiometric spinel ferrites and their catalytic activity*. Catal. Commun.140 (2020) 105986. https://doi.org/10.1016/j.catcom.2020.105986.

55. F.A Garcés-Pineda, M. Blasco-Ahicart, D. Nieto-Castro, et al. *Direct magnetic enhancement of electrocatalytic water oxidation in alkaline media*. Nat Energy 4, (2019) 519–525. https://doi.org/10.1038/s41560-019-0404-4.

56. J. Yu, J. Kiwi, I. Zivkovic, H.M. Rønnow, T. Wang, S. Rtimi, *Quantification of the local magnetized nanotube domains accelerating the photocatalytic removal of the emerging pollutant tetracycline,* Appl. Catal. B 248 (2019)450-458. https://doi.org/10.1016/j.apcatb.2019.02.046.